Boundary-Layer Meteorology (2006) 119: 81–107
DOI 10.1007/s10546-005-9010-z © Springer 2005

ON THE VARIABILITY OF THE FLUXES OF MOMENTUM AND SENSIBLE HEAT

WILLIAM M. DRENNAN* and LYNN K. SHAY
Rosenstiel School of Marine and Atmospheric Science, University of Miami, 4600 Rickenbacker Causeway, Miami, FL 33149, U.S.A.

(Received in final form 28 June 2005 / Published online: 30 December 2005)

Abstract. Direct measurements of the air–sea turbulent fluxes of momentum and heat, along with surface currents, waves and supporting meteorological variables, were acquired during a recent field campaign. Surface currents, measured from a very high frequency radar, were found to steer the stress away from the mean wind direction. Although this effect has been reported in a recent scatterometer study, this is the first time it has been observed in an *in situ* study with co-located flux, wind and surface current measurements. Data collected during a week of stationary conditions are used to investigate and quantify the sampling variability of the air–sea fluxes of momentum and sensible heat.

Keywords: Air–sea fluxes, Sampling variability, Stress direction, Surface currents, Wind stress.

1. Introduction

Many field experiments utilise a variety of instruments, often from several groups, to better understand the variability of key parameters. In comparing data from different sources, regression analysis remains the standard tool. However, the additional information contained in the scatter about the regression line is also significant in determining whether the two data sources agree. As discussed in Krogstad et al. (1999), the expected scatter is related to the sampling error of the sensors. If the sampling error is known, or can be estimated, error bars can be placed around the regression line, and a test can be made as to whether the observed scatter is consistent with that expected. This approach has been used to compare wave data from different sources (Krogstad et al., 1999; Pettersson et al., 2003), and also air–sea flux data with model predictions (Drennan et al., 2005).

However, such an approach requires estimates of the sampling errors. There have been very few field investigations into the accuracy of flux

* E-mail: wdrennan@rsmas.miami.edu

measurements; exceptions are the 1968 Kansas experiment (Wyngaard, 1973), the 1976 International Turbulence Comparison Experiment (Dyer et al., 1982), and the study of Sreenivasan et al. (1978; hereafter SCA78). The last study used observations collected from a tower in Bass Strait off the southern coastline of Australia to analyse the accuracy of the moments to order four of both velocity and scalar fluctuations, as well as their products, the turbulent fluxes. Under the assumption that the variables are Gaussian (or jointly Gaussian in the case of products) and stationary, they provide formulae for the expected variability due to sampling errors alone.

These error estimates, made using the hot wire and propeller anemometers of the time, have rarely been verified in the field. Exceptions are Donelan (1990) and Högström and Smedman (2004). Donelan found the variability of momentum flux (the only parameter tested) measured at a research tower in Lake Ontario to be 20% larger than the Sreenivasan estimate. Högström and Smedman (2004), comparing three instruments in both the field and laboratory, found much higher errors for the two sonic anemometers tested than for the 'MIUU' hot-film turbulence probe. The errors in momentum flux for the Gill R3 and R2 sonic anemometers were estimated to be respectively 70% and 54% higher than would be predicted by SCA78.

Here we revisit these estimates for both the momentum flux and heat flux using a new set of data collected using a sonic anemometer deployed on an air–sea interaction spar buoy. During a recent campaign, described in Section 2, a weeklong period of near stationary conditions was observed. The resulting dataset (Section 3) is unique in that all major forcing parameters (meteorology, buoyancy, waves and surface currents) were measured. Surface currents, although moderate, were found to exhibit a significant effect on the wind-stress direction. The fluxes and forcing variables are investigated for stationarity (Section 4), and new estimates are provided for sampling variability under stationary conditions.

2. The AWE Experiment

AWE, the Adverse Weather Experiment, took place off Ft. Lauderdale, Florida, U.S.A. during April–May 2000. The goal of the experiment, funded by the U.S. Office of Naval Research, was to investigate the impact of adverse weather fronts on air–sea interaction and mixing in the shallow water column over the continental shelf.

The specific objectives of AWE were, (i) to parameterise the vertical fluxes of heat and momentum and the turbulent kinetic energy dissipation rate in the upper oceanic mixed layer, and (ii) to parameterise the buoyancy and momentum fluxes in the marine atmospheric boundary layer.

To achieve the AWE objectives, measurements were conducted in the coastal waters off South Florida where the continental shelf is fairly narrow (less than 4 km) and is affected by both wind forcing and intermittent intrusions of the Florida Current. During AWE, the University of Miami Ocean Surface Current Radar (OSCR) system was deployed starting on 6 April (Julian Day 97) and ending on 15 May 2000 (JD136) in the South Florida Ocean Measurement Center, SFOMC (Venezia et al., 2003). The system consisted of two very high frequency (VHF) radar transmit/receive stations operating at 49.945 MHz that sensed the electromagnetic signals scattered from surface gravity waves with wavelengths of 2.95 m. The measurement represents the surface current in the upper 0.23 m at this frequency (Stewart and Joy, 1974). The VHF radar system mapped coastal ocean currents over a 7.5 km $\times$ 8 km domain with a horizontal resolution of 250 m at 700 grid points (Figure 1). Radar sites were located in John U. Lloyd State Park, adjacent to the U.S. Navy Surface Weapons Center Facility (master: 26°5.6′ N, 80°6.4′ W), and an ocean front site in Hollywood Beach, Florida (slave: 26°2′ N, 80°6.7′ W), equating to a baseline distance of 6.7 km. Each site consisted of a four-element transmit and thirty-element receiving array (spaced 2.95 m apart) oriented at an angle of 37° (south-west to north-east) at master and 160° (south-east to north-west) at slave. A total of 2755 vector 20-min current samples were acquired over the 38.25-day deployment period of which 122 samples (4.4%) were missing from the vector time series. This is consistent with previous VHF radar experiments in this domain (Shay et al., 2002; Martinez-Pedraja et al., 2004).

During AWE, a bottom-mounted upward-looking 300 kHz acoustic Doppler current profiler (ADCP) was deployed in the north-west portion of the radar domain at 11 m depth sampling the current vector between 2.5 and 9.5 m at 1-h intervals in the SFOMC (Soloviev et al., 2003). To facilitate direct comparisons, the 20-min sample interval of the VHF radar-derived currents was smoothed using a 3-point Hanning window and subsampled at hourly intervals to coincide with the ADCP measurements at 2.5-m depth (Figure 2). Time series indicated fairly energetic along-shelf currents (v) ranging from -0.30 to more than $0.45\,\mathrm{m\,s^{-1}}$. These strong northward excursions were associated with the western flank of the Florida Current where surface current vorticities scale as large as $7f$ where f is the local Coriolis parameter (Peters et al., 2002). Weaker cross-shelf (u) currents typically ranged between $\pm 0.15\,\mathrm{m\,s^{-1}}$. While there is fairly good agreement between the surface and 2.5-m currents, the weaker cross-shelf current components indicate more of a difference (Shay et al., 2002, 2003). Statistical comparisons are given in Table I between 2.5 and 9.5 m at the ADCP mooring relative to surface currents. The root-mean-square (*rms*) differences (2.5-m depth) of 0.074 and $0.053\,\mathrm{m\,s^{-1}}$ in the cross-shelf and

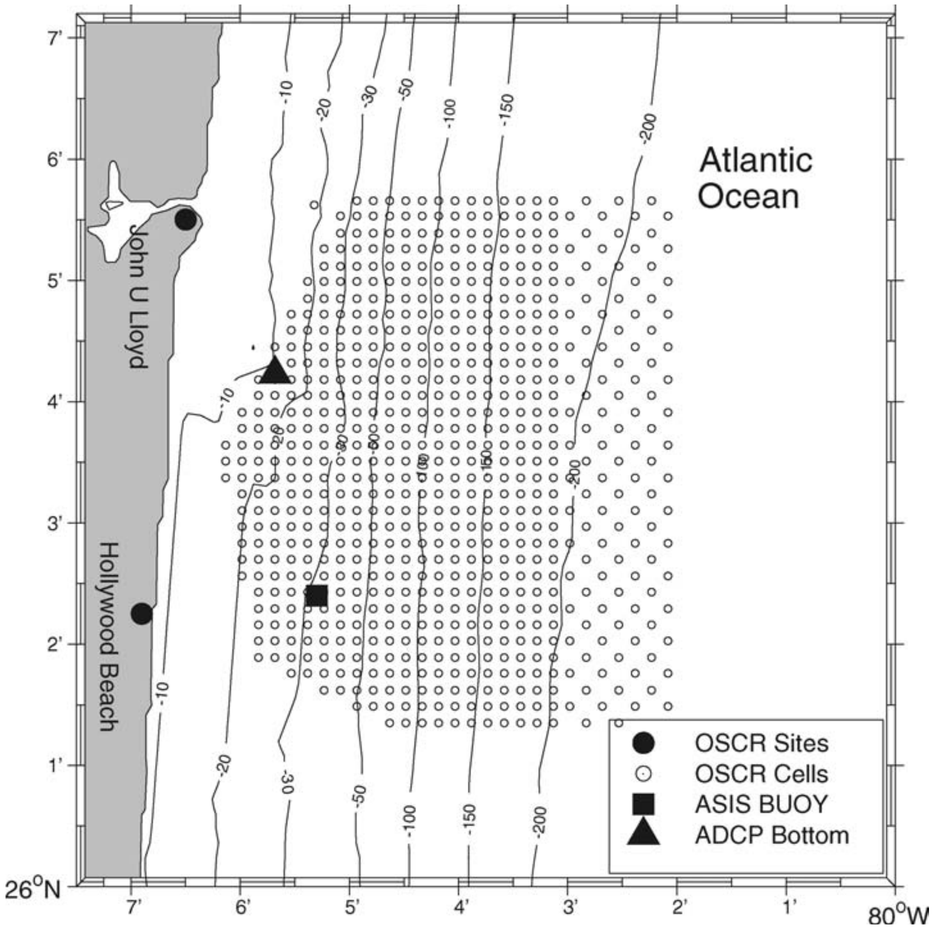

Figure 1. Location of the Adverse Weather Experiment in the South Florida Ocean Measurement Center off Ft. Lauderdale, Florida showing the OSCR cells (dots), bottom topography (contours in m), the ADCP mooring (triangle) deployed by Nova University in cooperation with the University of South Florida and the ASIS buoy (square). The master and slave sites for the VHF radar (black circles) were located at John U. Lloyd State Park and Hollywood Beach, respectively.

along-shelf directions, respectively are within cited accuracies of the instruments. In the along-shelf direction, differences between the surface and 2.5 and 9.5 m were 0.05–0.11 m s^{-1}, respectively. These values are consistent with previous studies given the energetic Florida Current structure that intermittently intrudes across the shelf break. Phase angles suggested a cyclonic veering with depth of the sub-surface current vector at 2.5 and 9.5 m relative to the surface velocity measurements at the ADCP mooring. Regression analysis (not shown) indicates considerably more scatter in the

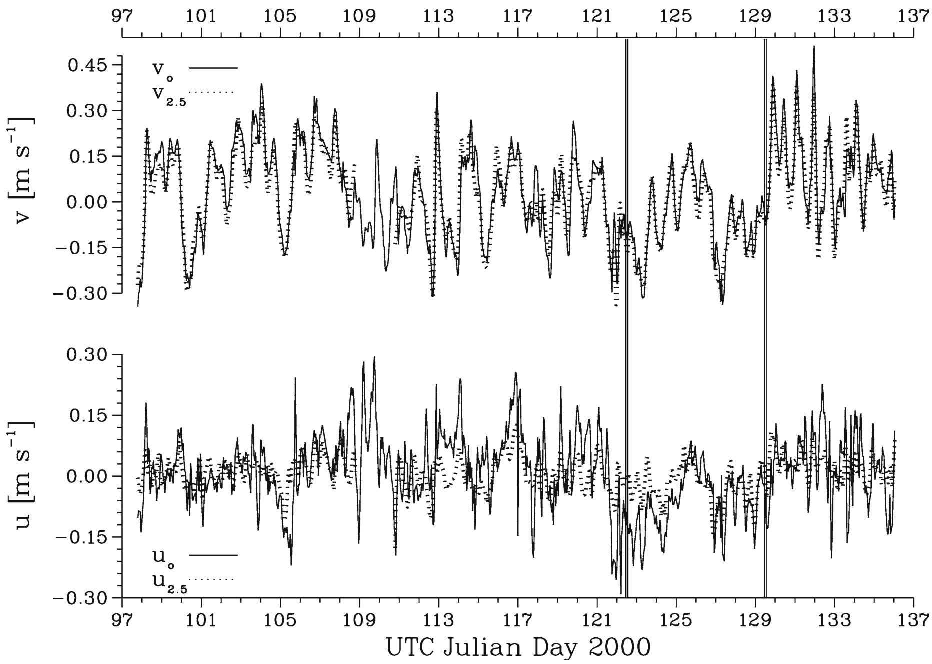

Figure 2. Comparison of along-shelf (v: top panel) and cross-shelf (u: bottom panel) currents from OSCR (solid) and 2.5 m (dotted) at the SFOMC 11 m mooring during the Adverse Weather Experiment. The analysis focuses on the period from JD 122.5 to 129.5. ADCP mooring data were missing between JD 108 and 110 for maintenance of the buoy.

TABLE I

Averaged difference between the surface and subsurface currents at 2.5 and 9.5 m for east-west (u_{o-b}) component, north-south (v_{o-b}) component, correlation coefficient (γ^2), phase (ϕ) and the *rms* differences in the east-west ($u_{o-b_{rms}}$) and north-south ($v_{o-b_{rms}}$) velocity components based on 872 hourly currents from the ADCP mooring at 11-m depth at SFOMC.

Series	u_{o-b}(mm s^{-1})	v_{o-b}(mm s^{-1})	γ^2	$\phi(^\circ)$	$u_{o-b_{rms}}$ (mm s^{-1})	$v_{o-b_{rms}}$ (mm s^{-1})
$\vec{V}_{2.5m}$	−1	−11	0.74	6.0	74	53
$\vec{V}_{9.5m}$	12	25	0.36	22.2	98	110

weaker cross-shelf than the along-shelf directions where slopes were O(1) for the 2.5-m comparisons.

An autonomous underwater vehicle, AUV (Dhanak et al., 2001), was used to make measurements of current profiles, conductivity, temperature and small-scale turbulence, including turbulent kinetic energy dissipation rates, in the survey region. The AUV operated during JD 99–100 and 109–110, covering the passage of two strong frontal systems through the area.

An air–sea interaction spar buoy, ASIS (Graber et al., 2000), was deployed to measure the air–sea turbulent fluxes of momentum and buoyancy, along with mean meteorological conditions and surface waves. ASIS was deployed at 26°2.4′ N, 80°5.43′ W, 2 km from the shore at a depth of 20 m. The mooring site was adjacent to the AUV survey area, and within the VHF radar domain. ASIS was deployed on JD 98, and operated continuously until recovery on JD 132.

3. ASIS Data

We focus primarily on the ASIS and OSCR data. During the 5-week experimental period, ASIS was instrumented as follows: a Solent 1012R2A sonic anemometer at 6.5-m above mean water level measured the three-dimensional wind vector and speed of sound; a pair of fast response thermocouples (6-m) measured air temperature; a Rotronic MP-100C (5-m) measured air temperature and relative humidity; an 8-gauge capacitance wave wire array provided surface elevation; three orthogonal Columbia Research Laboratory SA-307HPTX linear accelerometers, three orthogonal Systron Donner GC1-00050-100 rate gyros, and a Precision Navigation TCM-2 compass measured the six components of buoy motion; a SensorTek UCM-60DL current meter at −5 m measured currents, bulk water temperature and salinity. A second thermistor at −1 m failed. All instruments except the current meter were sampled continuously at 20 Hz for 60-min periods; the current meter sampling was set at 10 min. All data were subsequently analysed in 30-min blocks.

Following Anctil et al. (1994), the buoy motion measurements were used to correct the wind velocity vector (u, v, w, respectively the horizontal in-line with the mean wind, horizontal cross-wind and vertical wind components) to a stationary reference frame. The motion-corrected velocity data were then rotated into the mean wind direction (i.e. $\overline{v}=0$). A tilt correction, forcing $\overline{w}=0$, was also applied and linear trends were removed prior to estimating fluxes. Finally, the dataset was subject to quality control to remove runs where the wind direction was from the rear of the sonic (i.e. through the head supports). During AWE the data return rate for most sensors was near 100% throughout the deployment period. One signal needing slightly more attention was the speed of sound, which was affected by a narrow, but persistent, spike of unknown origin in the spectra at 0.182 Hz. This was removed by linearly interpolating through the spike in Fourier space. The speed of sound c is then converted to sonic temperature, $\theta_s=(c/20.067)^2$ and corrected for cross-wind contamination, following Kaimal and Gaynor (1991).

The stress vector $\hat{\tau}$ is calculated from the detrended turbulent velocity fluctuations as

$$\hat{\tau} = -\rho(\overline{w'u'}\hat{i} + \overline{w'v'}\hat{j}), \tag{1}$$

where the prime represents turbulent fluctuations, the overbar represents a time average of 30 min and ρ is the air density. The friction velocity is given by $u_* = (|\hat{\tau}|/\rho)^{1/2}$. To relate the measured 6.5-m winds to the standard 10-m neutral values, we assume a wind profile

$$U_z - U_0 = (u_*/\kappa)[\log(z/z_0) - \psi_u(z/L)] \tag{2}$$

using flux-profile relations ψ_u from Donelan (1990). Here U_0 represents the mean surface current in the wind direction (see below), $\kappa \approx 0.4$ is the von Kármán constant, z is the measurement height and z_o is the surface roughness length, or the height where the extrapolated wind profile crosses zero. The Obukhov length L is defined as

$$L = -u_*^3 \Theta_{\mathrm{v}} \, [\kappa g \overline{w'\theta'_{\mathrm{v}}}]^{-1}, \tag{3}$$

where Θ_{v} and θ'_{v} represent, respectively, the mean and turbulent components of virtual potential temperature, $\theta_{\mathrm{v}} = \theta(1 + 0.61q)$, θ is the potential temperature, q is the specific humidity, and g is the gravitational constant. Here we use the sonic temperature, $\theta_{\mathrm{s}} = \theta(1 + 0.52q)$, to calculate θ_{v}, making the small correction for humidity flux following Dupuis et al. (1997). Note, however, that Dupuis et al. use a slightly different definition for θ_{v} (Stull, 1988). This approach includes the effects of both humidity and temperature variations, and assumes equality of the bulk coefficients of heat and humidity. Typically the correction leads to changes in buoyancy flux (and L) of order 3%.

For comparison, we also compute L using a bulk heat flux parameterisation with constant Dalton and Stanton numbers equal to 0.0012 (Smith, 1989). The algorithm for L is iterative, and nonconvergent points are removed from the dataset. Both sonic and bulk $|L|$ are shown in logarithmic representation in Figure 3a, with negative (1326 points) and positive (72) values shown in grey and black, respectively. An additional 38 points are not shown in Figure 3a as the two estimates produce values of different sign. Much of the scatter in Figure 3a can be attributed to diurnal heating of the near-surface layer, which can result in the 5-m bulk water temperature estimate being of order 1 °C different from the true skin temperature (Katsaros, 1980). If only the nighttime data (from 0000 to 0800 local time) are included (panel b), the correlation for the unstable data improves (though not the few remaining stable cases).

A summary of meteorological conditions experienced during the AWE deployment is given in Figure 4. The atmospheric pressure (panel a)

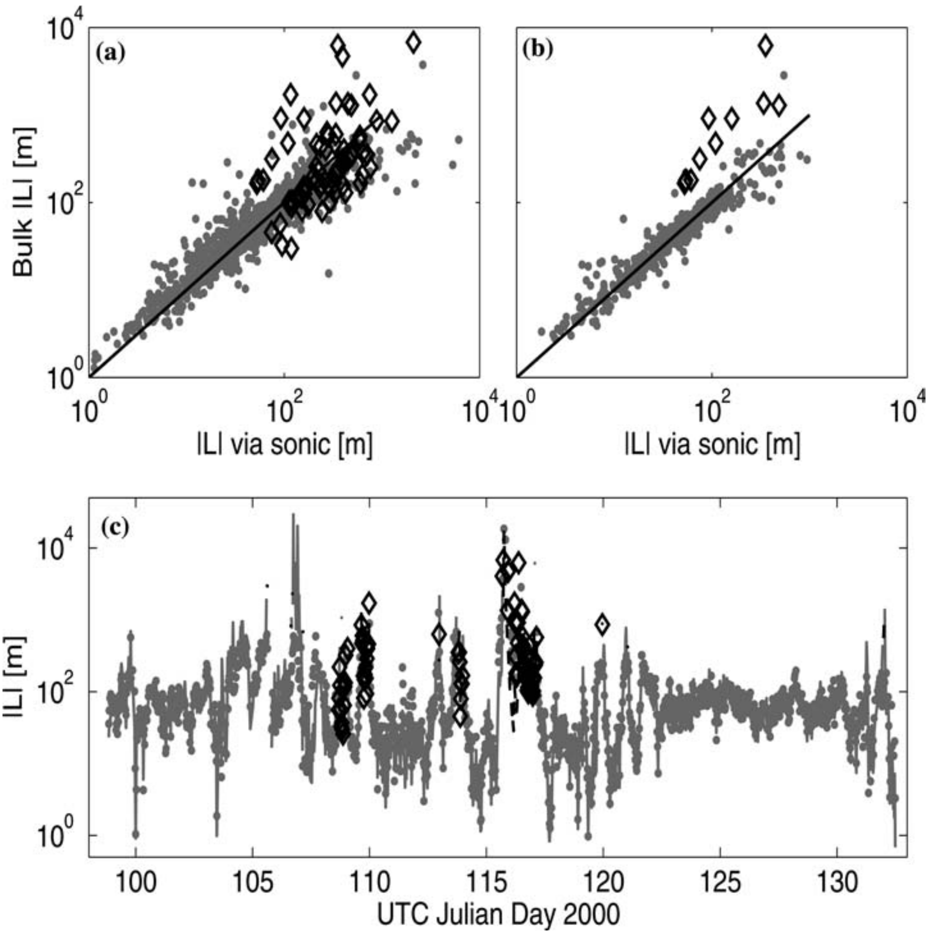

Figure 3. Obukhov length L calculated via the sonic heat flux and a bulk algorithm. Panel (a) shows a scatter plot of $\log(|L|)$, with unstable cases indicated with grey dots, and stable cases by diamonds. Panel (b) shows only the nighttime data. In panel (c), the two estimates are plotted as time series, with sonic values shown with lines (grey solid = unstable; black dashed = stable), and bulk estimates with symbols (grey $\bullet$ = unstable; black $\diamond$ = stable).

from the National Data Buoy Center's C-Man station at Fowey Rocks (FWYF1), 50 km south of ASIS, shows the seasonal transition: during the first three weeks (JD 98–115), cold fronts accompanying continental low pressure systems propagate through the region roughly every five days. By early May, the fronts no longer extend into southern Florida, leaving the region in the subtropical climate regime. The weather is then characterised by strong diurnal variations (JD 116–122), followed by onshore flow resulting from a stationary anticyclone to the north-east. The winds (panels b, c) are mostly moderate, reaching a maximum of 12 m s^{-1}during the first frontal passage. The wind direction varied considerably during the first three weeks (north-west during the frontal passages, followed by a slow backing to the east), but was mainly easterly (onshore) towards the end of the experiment. The winds at Fowey Rocks, measured at 43.9 m, are also shown. For comparison the wind speed representative of the 6.5-m ASIS height is shown, and is calculated by application of Equation (2), using measured ASIS friction velocities. Agreement with the ASIS winds is excellent, indicating the homogeneity of the site. For the most part, the atmospheric boundary layer is slightly unstable, with an Obukhov length of order -50 m (Figure 3c). The ASIS relative humidity measurement (Figure 4d) underwent a sudden offset during JD 105; and data after that time were corrected upwards by 22%. The correction was checked against

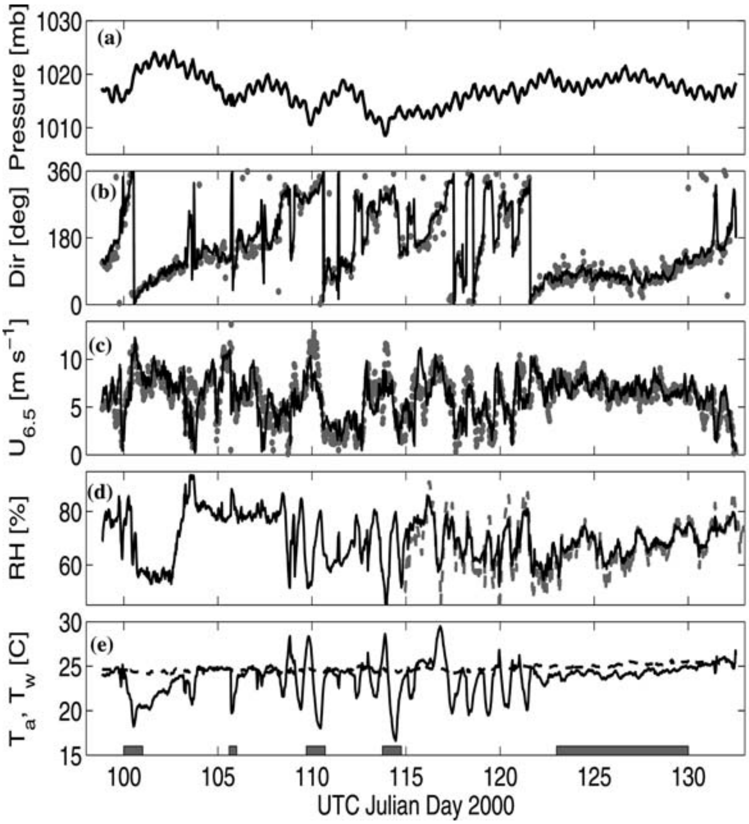

Figure 4. Summary of meteorological conditions during AWE. The panels show: (a) atmospheric pressure from the Fowey Rocks C-Man station (FWYF1); (b) wind direction from ASIS and Fowey Rocks (•); (c) 6.5-m wind speed from ASIS and Fowey Rocks (•, reduced from 43 m); (d) relative humidity from ASIS and the Dania Pier (dashed, from JD 115); (e) air and water (dashed) temperatures from ASIS. The first four events indicated by shading are cold front passages; the last is a stationary high pressure region.

humidity from a meteorological package at the Dania pier, several km north-west of the site (also shown on the plot).

Five periods are identified by shading in Figure 4e. The first four are associated with the passage of cold fronts through the domain, with each frontal passage marked by a local pressure minimum, a turning of the wind to the north-west, and a fall in air temperature (panel e). For the stronger fronts, the relative humidity also fell significantly. AUV operations were carried out during the first and third frontal passages. The fifth period, during days 122–129, is associated with a stationary high pressure region to the north-east of the domain. These periods, typical during the southern Florida spring season, are known for their persistent and steady winds.

Six capacitance wave staffs, each 3.5 m long by 0.9 mm in diameter, were deployed on ASIS: five in a pentagon of radius 0.93 m along the outer perimeter of the buoy, and a further one in the centre. Several wave staffs failed during the course of the experiment, but at least three were available at all times. The surface elevation measurements are corrected for platform motion following Drennan et al. (1994) and Pettersson et al. (2003); a summary of the wave conditions as measured from ASIS is given in Figure 5. For the most part, the waves are small and near full development, with significant wave height H_s approximately 1 m, and inverse wave age u_*/c_p around 0.04 ($U_{10N}/c_p \approx 1$). The evolution of the one-dimensional spectrum

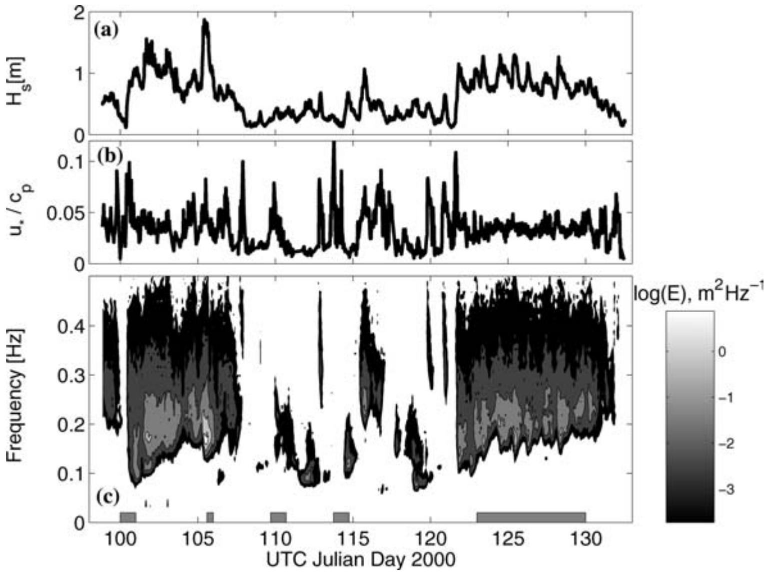

Figure 5. Summary of wave conditions during AWE. The panels show: (a) significant wave height, H_s; (b) inverse wave age, u_*/c_p, where u_* is the friction velocity and c_p the peak wave phase speed; (c) evolution of the one-dimensional wave spectrum, shaded to indicate spectral energy E. The five shaded areas denote events identified in Figure 4.

is shown in Figure 5c, where logarithmic contour intervals are used to emphasize the higher frequency waves. The response of the wave field to sudden increases in wind speed is readily seen by the appearance of high frequency wind waves, and also by the sudden increase in u_*/c_p (note, e.g., JD 113).

Directional wave spectra are calculated from the array data using the maximum likelihood method (Capon, 1969). A wave partitioning algorithm based on Gerling (1992) was applied to the directional wave spectra to determine the various components of the wave field. The energy, peak frequency, and mean propagation direction of each component are identified. A single component, meeting criteria $U_{10N}\cos(\phi_d) > 0.83c_p$ (Donelan et al., 1985) and $|\phi_d| < 45°$, where ϕ_d is the mean angle between the wind and waves, is identified as wind sea; other components are identified as swell. During AWE, the wave field was for the most part unimodal, usually wind waves, or, in a decaying or low wind, recent and short-lived swell.

The surface current magnitudes and directions from the VHF cell nearest ASIS are plotted in Figure 6; the mean current magnitude was $U_c = 0.17 \pm 0.10\,\mathrm{m\,s^{-1}}$(one standard deviation). Several different current scenarios were observed during AWE. During shoreward incursions of the Florida Current, currents at ASIS were northward (shore-parallel) and independent of the wind field; this occurred over 40% of the time. When the Florida Current was offshore, currents were often in the wind direction ($|\phi_c| < 30°$ for 30% of the time, where ϕ_c is the current direction relative to that of the wind), and presumably wind driven (e.g. JD 98–101). On several days (e.g. JD 105) a southward near-shore current was observed (17%), while on JD123 an eddy

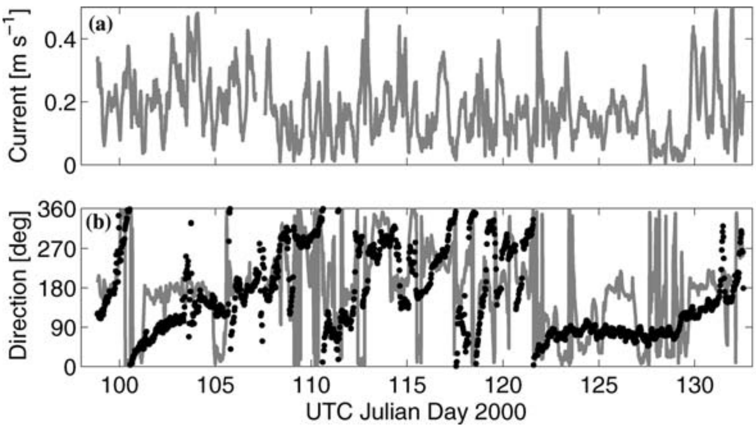

Figure 6. Currents during AWE. Panel (a) shows the surface current magnitude at the OSCR cell nearest the ASIS mooring. Panel (b) shows the OSCR current direction and the ASIS wind direction (•).

passed through the domain. For future reference, we define $U_0 = U_c \cos(\phi_c)$, the component of surface current in the mean wind direction.

Surface current measurements revealed complex surface features with frequent Florida Current intrusions and multiple current reversals (Shay et al., 2002, 2003; Martinez-Pedraja et al., 2004). An example of the variability over a three-day period, JD 124–127, is shown in Figure 7. On JD 124–125 there is a general south-westerly to southerly current over the inner shelf where currents range between 0.25 and 0.40 m s^{-1}. In the south-east part of the radar domain, there is evidence of cyclonic turning of the surface current vectors. By 1800 UTC, the Florida Current moved westward and impacted the inner shelf with northward currents of 0.40 m s^{-1}. Further offshore, surface velocities associated with the Florida Current's western flank exceeded 1 m s^{-1}. This trend continued into JD 126, however inner-shelf currents of 0.20–0.30 m s^{-1} also indicated a wave-like structure and a surface convergence zone. These wave-like features have periods of ≈10 h and are usually associated with significant vorticity (Peters et al., 2002). Nine hours later, the Florida Current meandered eastward, however surface currents remained towards the north with a maximum velocity of 0.75 m s^{-1}. On JD 127, currents were weaker with a magnitude of ≈0.40 m s^{-1}. A convergence zone

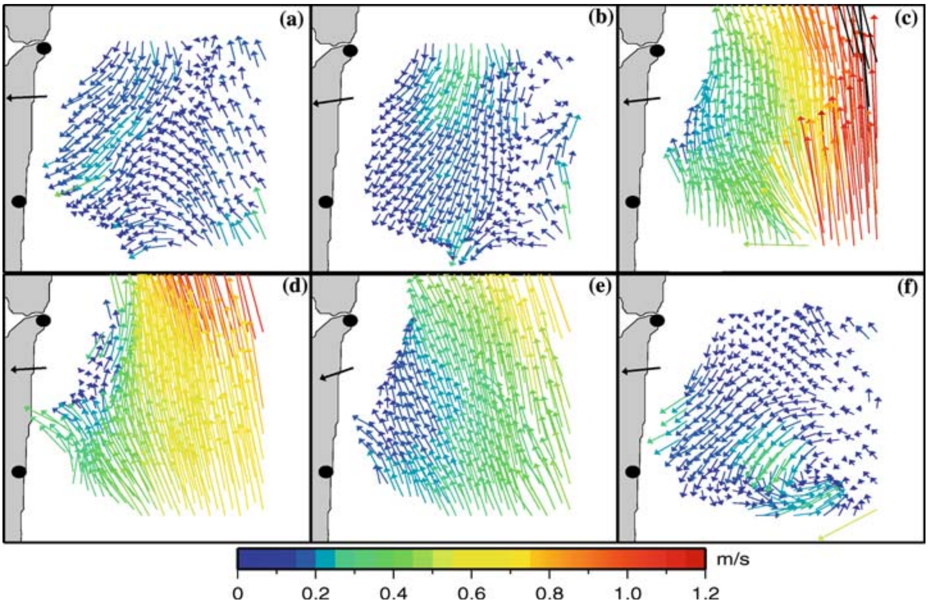

Figure 7. Surface current evolution in the VHF-radar domain observed during AWE from (a) JD 124, 0000 UTC; (b) JD 125, 0000 UTC; (c) JD 125, 1800 UTC; (d) JD 126, 0100 UTC; (e) JD 126, 1000 UTC; (f) JD 127, 0100 UTC. The colour bar provides the magnitude of the surface currents. Wind direction from Dania Pier is shown as a black vector along the coast and the VHF radar master and slave sites are shown as black dots as per Figure 1.

developed as a result of southward inner-shelf currents and a cyclonic vortex with a scale of a few km located offshore in the south-east part of the domain. Note that the Florida Current was well offshore during this day.

4. Fluxes and Variability

The covariance kinematic heat fluxes $\overline{w'\theta'}$ and $\overline{w'\theta'_s}$ are shown in Figure 8. Here the sensible heat flux is calculated from the sonic temperature flux according to

$$\overline{w'\theta'} = \overline{w'\theta'_s}(1 + 0.52Q_{10N} + 0.52\Theta_{10N}(Q_0 - Q_{10N})/\Delta\Theta)^{-1} \tag{4}$$

(Dupuis et al., 1997), where $\Delta\Theta = \Theta_0 - \Theta_{10N}$ and the mean surface specific humidity Q_0 is calculated from Θ_0 assuming saturation. Roughly 110 data points out of the 1550 total, mostly those with small $\Delta\Theta$, misbehaved during this correction, and were eliminated; the singularity results from the denominator of Equation (4) being near its zero value – errors in Θ_0 (and therefore Q_0) due to diurnal heating compound the problem. In applying Equation (4), a threshold value must be applied to the denominator to

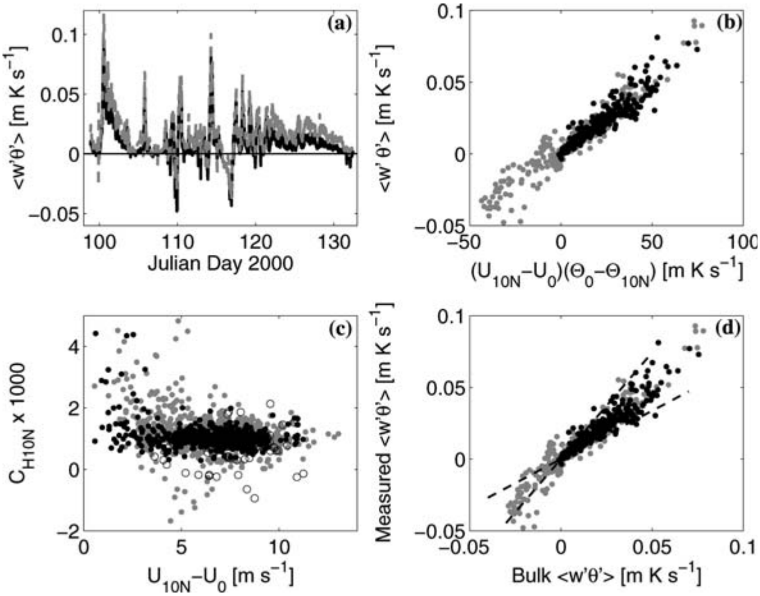

Figure 8. Heat flux during AWE. Nighttime data are shown with black dots. Panel (a) shows the covariance fluxes of temperature θ and sonic temperature θ_s (grey dashed). Panel (b) shows flux $\overline{w'\theta'}$ versus $(U_{10N} - U_0)(\Theta_0 - \Theta_{10N})$. Panel (c) shows the Stanton number versus wind speed. Circles indicate stable conditions. Panel (d) shows bulk versus measured heat flux. The dashed lines represent 90% confidence limits based on the measured sampling variability.

eliminate singular values. This correction, which assumes that the bulk heat and humidity coefficients are equal, is roughly 20% during unstable conditions, double that found by Schotanus et al. (1983) over land. The sonic anemometer was found to give consistent sensible heat estimates even for low values. This is somewhat surprising, given the high noise levels of the anemometer measured speed of sound c, even after the gain of 5 applied to the channel before recording.

To assess the sonic anemometer for heat flux measurements, a pair of thermocouples was deployed 0.5 m below the anemometer head. The thermocouple system, designed for wet/dry bulb measurements (Katsaros et al., 1993), was deployed here with a pair of 50-μm diameter copper–constantan dry bulb sensors, separated by 40 mm. Under the assumption that salt particles would rarely impact the two sensors at the same time, the pair were analysed together using a difference algorithm to remove salt-based spikes. Unfortunately, the gain on the thermocouple electronics slowly drifted during the course of the experiment. Hence we are able to use only the spectral information from the thermocouples, but not the absolute values. In Figure 9, we compare spectra from the corrected thermocouple with the sonic temperature for three representative times. Although sonic temperature includes humidity as well as temperature, we expect the θ_s and θ spectra and cospectra (with w) to be similar in shape due to the typical spectral similarity between θ and q at low to moderate wind speeds (but, see Katsaros et al., 1993 for the discussion of an exceptional case).

The top panels show the temperature spectra for unstable cases with strong forcing, ($\Delta\Theta = 9.2$ K, $\Delta U = U_{10N} - U_0 = 5.2\,\mathrm{m\,s^{-1}}$, on JD 114.45, left) and weak forcing ($\Delta\Theta = 0.5$ K, $\Delta U = 2.9\,\mathrm{m\,s^{-1}}$on JD 119.66, middle), and a stable case ($\Delta\Theta = -3.9$ K, $\Delta U = 9.5\,\mathrm{m\,s^{-1}}$on JD 109.81, right). In each case, the thermocouple spectra $S_{\theta\theta}$ (black curves), which are multiplied by 0.1, are seen to exhibit the expected inertial subrange slope of $f^{-5/3}$. In the strongly forced case, the sonic temperature spectrum also exhibits a well-defined inertial subrange; however high noise levels limit the θ_s inertial subrange range for most other cases. Hence, as noted by Dupuis et al. (2003), the sonic temperature is not generally suitable for heat flux measurements via the inertial dissipation method.

The cospectra $S_{w\theta}$ and $S_{w\theta s}$ are presented in the middle row, where we have normalised the thermocouple cospectra so that the spectra match for frequencies around 0.1 Hz. Again, this assumes similarity of the humidity and temperature spectra. Although $S_{w\theta s}$ clearly shows more noise at higher frequencies, the cumulative cospectra, normalised to 1 (lower panels) are in excellent agreement. The sonic temperature noise at high frequencies increases considerably as the forcing decreases. Nevertheless, even for weak forcing, both the spectra and cospectra agree well for lower frequencies,

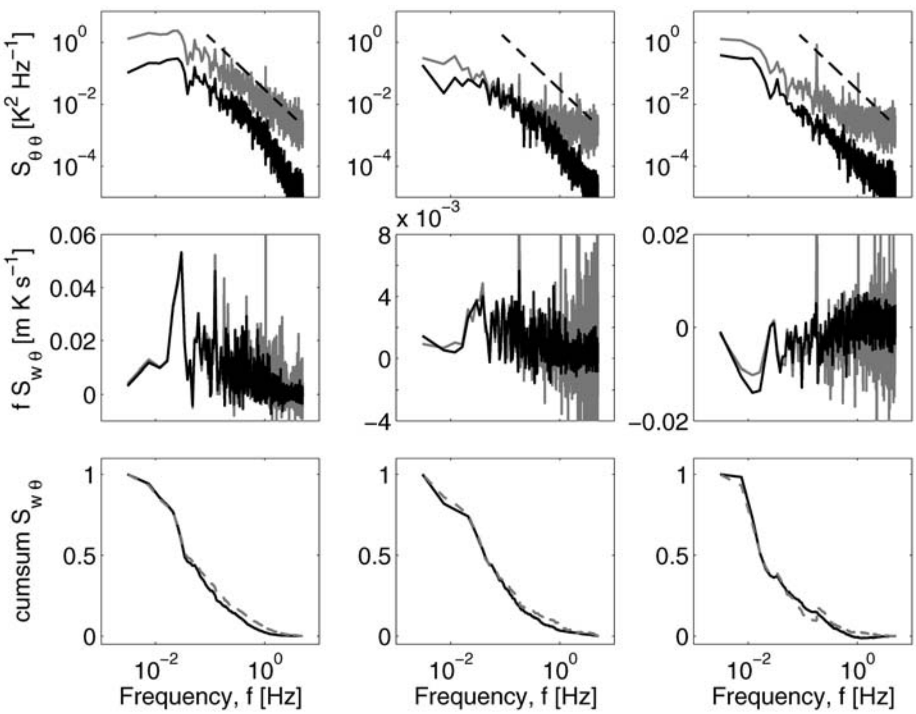

Figure 9. Temperature spectra (top) and cospectra (middle) from a thermocouple (black) and sonic anemometer. The bottom panels show the cumulative cospectral sums, normalised to 1. The three cases are from JD 114.45 (left, strongly unstable), JD 119.66 (centre, weakly unstable), and JD 109.81, (moderately stable). In the top panels, the thermocouple spectra are divided by 10; the dashed lines show the expected inertial subrange slope $f^{-5/3}$. In the middle panels, the thermocouple gains have been normalised to match the sonic temperature around 0.1 Hz.

while the cumulative cospectra are in good agreement at all frequencies. The stable case (third column) agrees qualitatively with the low forcing case: while the sonic temperature signal is noisy at higher frequencies, the cospectra, and especially the cumulative cospectra, are in good agreement.

Hence we conclude that the high frequency noise experienced with the sonic temperature (after a gain of 5) does not preclude good eddy correlation heat flux measurements. This is consistent with Högström and Smedman (2004), and also Pedreros et al. (2003). As seen in Figure 8b, where $\overline{w'\theta'}$ is plotted against $\Delta U \Delta\Theta$, the unstable data pass through zero with no increase in scatter for small $\Delta U \Delta\Theta$. Hence unlike most earlier studies, we do not apply a threshold on $\Delta\Theta$ in using the data. The stable data are not as well behaved, but as these are mostly daytime cases the error is likely in $\Delta\Theta$, which uses a bulk (−5 m) value for Θ_0.

In Figure 8c, the Stanton number

$$C_H = C_{H10N} = \overline{w'\theta'}[(U_{10N} - U_0)(\Theta_0 - \Theta_{10N})]^{-1} \quad (5)$$

is plotted against relative wind speed ΔU. For the nighttime data with $\Delta U > 3\,\mathrm{m\,s^{-1}}$(441 points, all unstable) $C_H = (1.01 \pm 0.03) \times 10^{-3}$, showing two standard errors, with no significant wind speed dependence. The nighttime C_H does not show a significant dependence on stability parameter z/L (not shown), although the C_H values nearest neutral, $-0.05 < z/L < 0$, are on average 20% lower than other values. For the full dataset, again with $\Delta U > 3\,\mathrm{m\,s^{-1}}$, $C_H = (1.09 \pm 0.03) \times 10^{-3}$ (1255 points) for unstable conditions and $C_H = (0.69 \pm 0.13) \times 10^{-3}$ for stable conditions (65 points). These data support those of other recent experiments, including Large and Pond (1982), DeCosmo et al. (1996) and Larsén et al. (2004), with constant Stanton numbers for unstable and stable conditions, and the mean stable C_H lower than the mean unstable C_H. Given the uncertainty with daytime water temperatures, we consider the nighttime C_H estimate to be more reliable for unstable conditions. Although the stable C_H value is consistent with other estimates (e.g. Large and Pond, 1982; Larsén et al., 2004) it may be biased due to diurnal heating.

The two components of momentum flux are plotted in Figure 10a. For the most part, the along-wind component $-\overline{w'u'}$ dominates the cross-wind component $-\overline{w'v'}$. The stress angle $\phi_\tau = \tan^{-1}(-\overline{w'v'}/-\overline{w'u'})$ with respect to the mean 6.5-m wind is plotted in Figure 10b, along with the angle of the surface current with respect to mean wind, ϕ_c (only when $U_c > 0.1\,\mathrm{m\,s^{-1}}$and $U_{10N} > 6\,\mathrm{m\,s^{-1}}$). The correlation between the two angles is 0.53. In these moderate winds and currents, the stress vector is usually oriented between the 6.5-m wind and current directions. Consider, for instance, the period JD 124.5–127.5, which includes a significant change in relative current angle during JD 125–127, as the Florida Current intruded shoreward (Figure 7).

The wind, stress and current variations during these three days are shown in Figure 11. Prior to the current intrusion, both the current and stress angles were aligned roughly with the wind: $\phi_c = -13 \pm 10^\circ$ and $\phi_\tau = 5 \pm 3^\circ$ (showing two standard errors). During the 42-h intrusion event, the current was perpendicular to the wind, $\phi_c = 94 \pm 5^\circ$, with the stress angle between the wind and current angles: $\phi_\tau = 28 \pm 4^\circ$.

The eastward retreat of the Florida Current late on JD 126 marked the end of the event, and was followed by the passage of an eddy through the domain around 0000 UTC on JD 127. Note the current reversal relative to the near-steady wind direction in Figure 11b. The wind stress direction follows the change in the current direction, before relaxing to the wind direction as the eddy passes. The correlation coefficient between ϕ_c and ϕ_τ during this period is 0.66. However, as seen around JD 125.8, other factors are also present: for a few hours at the peak of the event the cross-wind

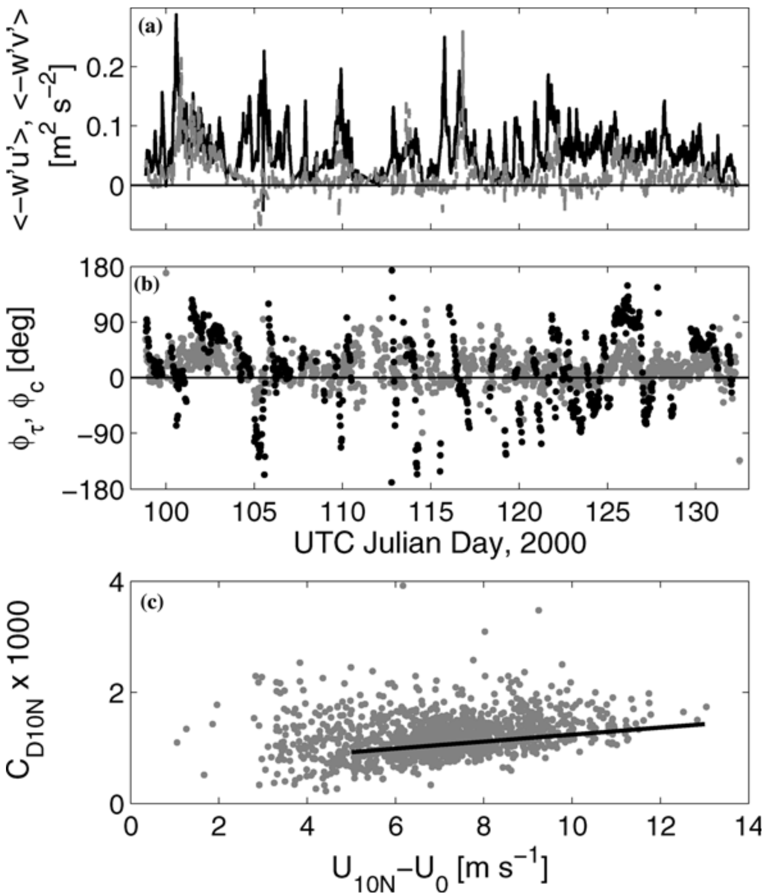

Figure 10. (a) Along-wind $-\overline{w'u'}$ and cross-wind $-\overline{w'v'}$ (dashed grey) momentum flux components. (b) Stress angle $\phi_\tau = \tan^{-1}(\overline{w'v'}/\overline{w'u'})$ (grey) and surface current angle ϕ_c relative to the wind. The latter is plotted only when $U_c > 0.1$ and $U_{10N} > 6\,\mathrm{m\,s^{-1}}$. (c) Neutral drag coefficient versus wind speed; the straight line is from Smith (1980).

stress reduces, and the relative stress direction becomes zero. This short-lived period occurs after 12 hrs of gradually declining winds (from 9 to $6\,\mathrm{m\,s^{-1}}$) during which the wave age exceeds full development. Unfortunately our wave measurements do not extend to 10-mm scale wavelengths where the stress is supported. Hence we can only speculate that the effect is due to the wave field. This remains a subject for future research.

That the stress direction is often different from that of the wind has been known for some time. Studies using scatterometer data have used this fact to infer information about the ocean surface. While the standard scatterometer product is the wind field, in fact the radar responds to the short waves that carry the stress, and so the backscatter is more closely related to the stress. Cornillon and Park (2001) used the difference between the wind

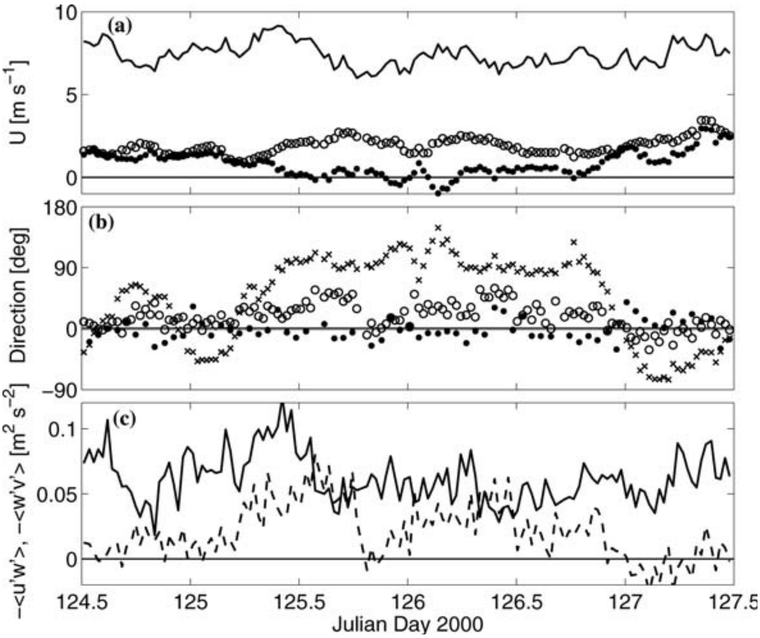

Figure 11. (a) Wind speed U_{10N}, current speed ($\times 10$, $\circ$), current component in wind direction U_0 ($\times 10$, $\bullet$); (b) relative directions of the stress vector ($\circ$), peak waves ($\bullet$) and surface current ($\times$) with respect to the wind; (c) along-wind $-\overline{w'u'}$ (solid) and cross-wind $-\overline{w'v'}$ (dashed) stress components during period of an intrusion of the Florida Current.

vector measured by the scatterometer and the presumably homogeneous local wind field to infer the surface current velocities associated with Gulf Stream eddies.

Other studies have attributed the differences between the wind and stress directions to coastal jets (Zemba and Friehe, 1987), surface heat flux (Geernaert et al., 1988), or the direction of long waves or swell (Geernaert et al., 1993; Rieder et al., 1994; Grachev et al., 2003). However, here these effects were either absent (there was little or no swell; coastal jets are unlikely in onshore flow) or not correlated with ϕ_c (the correlation of surface heat flux with ϕ_c is only $\gamma^2 = 0.09$).

To the authors' knowledge, the AWE data are the first *in situ* data to support the bulk-derived estimates of Halpern (1988) that surface currents steer the wind stress. Few studies of wind stress include current measurements; coincident surface current measurements are even rarer. It seems likely that unobserved variations in surface current result in some of the scatter in ϕ_τ found in previous studies. This demonstrates the need for near-surface current as well as wave measurements in such studies.

The neutral 10-m drag coefficient,

$$C_D = C_{D10N} = u_*^2/(U_{10N} - U_0)^2, \tag{6}$$

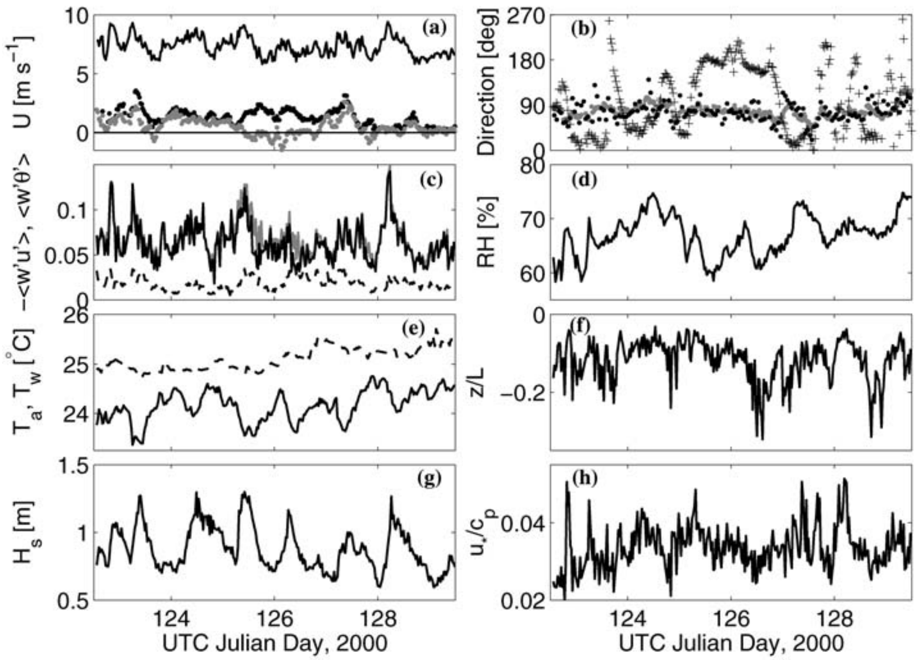

Figure 12. Conditions during stationary period: (a) Wind speed U_{10N}, current speed ($\times 10$, black •), current component in wind direction U_0 ($\times 10$, grey •); (b) direction of wind (grey •), peak waves (black •) and current (+); (c) along-wind momentum flux $-\overline{w'u'}$ ($m^2\,s^{-2}$, black solid), momentum flux magnitude u_*^2 ($m^2\,s^{-2}$, grey), and heat flux $\overline{w'\theta'}$ ($\times 2$, $m\,K\,s^{-1}$, dashed); (d) relative humidity; (e) air and water (dashed) temperatures; (f) stability parameter, z/L; (g) significant wave height, H_s; (h) inverse wave age, u_*/c_p.

is plotted against relative wind speed in Figure 10c. The plot exhibits a general agreement in the mean with the classic Smith (1980) and other relationships, with a considerable amount of scatter. One goal here is to assess how much of the observed scatter or variability arises from geophysical forcing as opposed to statistical uncertainty. Here we focus on the week-long period from JD122.5–129.5, when a stationary anticyclone over the Atlantic to the north-east of the study site resulted in a steady onshore flow ($U_{10N} = 7.55 \pm 0.80\,m\,s^{-1}$from $78 \pm 13°$, showing one standard deviation) and slightly unstable conditions ($\Delta\Theta = 1.08 \pm 0.33\,°C$; $z/L = -0.12 \pm 0.05$). The waves were moderate $H_s = 0.88 \pm 0.16\,m$, near full development ($U_{10N}\cos\phi_d/c_p = 0.95 \pm 0.15$ or $u_*/c_p = 0.034 \pm 0.006$) and propagating in the wind direction $76 \pm 20°$. There was little or no swell. The primary variability in each of these parameters is diurnal, with the wind increasing somewhat during the local afternoon. The surface current was moderate ($U_c = 0.13 \pm 0.07\,m\,s^{-1}$), with variable direction. See Figure 12 for a summary of the fluxes and forcing variables during this period.

TABLE II

Analysis of fluxes and second-order moments during stationary period of JD 122.5–129.5. The first three columns are: parameter X, standard deviation of X, and standard deviation of X divided by mean of X. The last seven columns are the correlation coefficient of X with: relative wind speed ($\Delta U = U_{10N} - U_0$), current magnitude U_c and direction relative to the wind θ_c, significant wave height H_s, inverse wave age u_*/c_p, stability z/L and air-sea temperature difference $\Delta\Theta = \Theta_0 - \Theta_{10N}$. Parameters with subscript B are residuals after subtraction of bulk estimates based on ΔU (σ_u, σ_w, $-\overline{w'u'}$, u_*^2), $\Delta\Theta$ ($\sigma_{\theta s}$) or $\Delta\Theta\Delta U$ ($\overline{w'\theta'}$), or after the removal of days JD 125.25–127 with anomolous cross currents (σ_v, $-\overline{w'v'}$). The parameters with subscript A are residuals after removal of wave-age dependent estimates. (*) Since mean($-\overline{w'v'}$)≈ 0, $\sigma_X/\overline{X}$ estimates for $-\overline{w'v'}$ use the mean of $-\overline{w'u'}$.

Parameter	σ_X	$\sigma_X/\overline{X}$	Correlation γ^2 of first column parameter with						
			ΔU	U_c	θ_c	H_s	u_*/c_p	z/L	$\Delta\Theta$
σ_u	0.097 m s^{-1}	0.14	0.63	0.26	0.08	0.31	0.33	0.33	0.31
σ_v	0.153 m s^{-1}	0.20	0.22	0.06	0.23	0.16	0.18	0.06	0.32
σ_w	0.032 m s^{-1}	0.10	0.90	0.15	−0.17	0.47	0.55	0.52	0.21
$\sigma_{\theta s}$	0.020 K	0.10	0.17	0.26	0.23	0.22	−0.06	−0.32	0.72
σ_{uB}	0.075 m s^{-1}	0.11	0.00	0.17	0.24	−0.03	0.02	0.03	0.31
σ_{vB}	0.133 m s^{-1}	0.19	0.32	−0.14	0.01	0.16	0.24	0.22	0.28
σ_{wB}	0.014 m s^{-1}	0.044	0.00	−0.06	−0.07	0.01	0.23	0.18	0.23
$\sigma_{\theta sB}$	0.014 K	0.071	0.12	0.00	0.37	0.19	−0.06	−0.22	0.00
$-\overline{w'u'}$	0.020 m^2 s^{-2}	0.32	0.80	0.02	−0.22	0.40	0.70	0.70	0.06
$-\overline{w'v'}$	0.019 m^2 s^{-2}	0.30*	0.03	−0.09	0.46	0.19	0.11	0.12	0.11
$\overline{w'\theta'}$	0.0035 m K s^{-1}	0.38	0.35	0.32	−0.04	0.27	0.06	−0.26	0.81
$-\overline{w'u'}_B$	0.012 m^2 s^{-2}	0.19	0.01	−0.21	−0.08	−0.02	0.50	0.52	−0.06
u^2_{*B}	0.012 m^2 s^{-2}	0.19	−0.02	−0.15	0.12	0.06	0.47	0.50	0.05
$-\overline{w'u'}_A$	0.010 m^2 s^{-2}	0.17	0.18	−0.07	−0.11	0.23	0.21	0.49	0.02
u^2_{*A}	0.011 m^2 s^{-2}	0.17	0.13	−0.01	0.12	0.37	0.17	0.46	0.14
$-\overline{w'v'}_B$	0.015 m^2 s^{-2}	0.23*	−0.08	−0.38	0.39	−0.02	0.10	0.15	−0.14
$\overline{w'\theta'}_B$	0.0018 m K s^{-1}	0.20	0.02	0.01	0.08	0.08	−0.07	−0.41	0.11

It is evident that the majority of variability present in the along-wind stress (Figure 12c) $-\overline{w'u'}$ arises from changes in the wind field, ΔU. Indeed the correlation between the two is 0.80, see Table II. High correlations with other variables such as H_s are likely to be spurious in that both $-\overline{w'u'}$ and H_s are related to the wind speed. We remove the wind speed correlation by subtracting from the stress the bulk estimate calculated using the Smith (1980) drag coefficient, that is

$$-\overline{w'u'}_B = -\overline{w'u'} - C_D(\Delta U)^2. \tag{7}$$

The standard deviation of the residual $-\overline{w'u'}_B$ is 40% less than that of $-\overline{w'u'}$. The correlation coefficients of $-\overline{w'u'}_B$ with the various forcing parameters are given in Table II. The correlations between $-\overline{w'u'}_B$ and wind speed or H_s are no longer significant but there remains a relatively high correlation $\gamma^2 = 0.5$ between $-\overline{w'u'}_B$ and inverse wave age u_*/c_p, despite the relatively small range of wave age during the stationary period. This effect of wave age on stress was first reported by Kitaigorodskii and Volkov (1965), and is now well known. To remove the wave-age dependence, we subtract from $-\overline{w'u'}$ the stress estimated using the Drennan et al. (2003) wave-age relation. This relation, $z_o/H_s = 3.35(u_*/c_p)^{3.4}$, gives the roughness length z_o, from which u_* is calculated using Equation (2). Here we assume that the wave-age relation gives the in-line component of stress. The standard deviation of the resulting wave age residual $-\overline{w'u'}_A$ is 20% lower than that of the bulk residual, and half that of the original $-\overline{w'u'}$ (Table II).

A similar investigation of heat flux shows that most of the variability in $\overline{w'\theta'}$ is associated with $\Delta\Theta$. We remove this from the flux by subtracting the bulk estimate,

$$\overline{w'\theta'}_B = \overline{w'\theta'} - 0.001\Delta U \Delta\Theta. \tag{8}$$

Again, the standard deviation is reduced by almost half.

The highest remaining correlation of the $\overline{w'\theta'}_B$ and $\overline{w'u'}_A$ residuals is with stability parameter z/L ($\gamma^2 = -0.41, 0.46$ respectively). This might arise from the profile relations used in arriving at the neutral wind and temperature estimates. However, a plot of the residuals versus z/L does not indicate any clear relation (not shown). Thus no attempt was made to remove this effect.

The variability of the cross-wind stress is mostly associated with variability in the current direction ($\gamma^2 = 0.46$), primarily during JD 125.2–127.5. In the analysis below, we omit this 50-h segment in considering $-\overline{w'v'}$, referring to the covariance excluding the period as $-\overline{w'v'}_B$. The period is retained for the in-line stress and heat flux, as its inclusion has no effect on the results.

In a similar fashion, we investigate the variability in the standard deviations of u, v, w and θ_s during this stationary period. Again finding much of the variability to be associated with variations of a forcing parameter, we remove linear trends of ΔU from σ_u and σ_w, a linear trend of $\Delta\Theta$ from $\sigma_{\theta s}$, and the period with currents perpendicular to the wind from σ_v. These are indicated with subscript B in Table II.

We now consider the variability of the residuals, $-\overline{w'u'}_A$, $-\overline{w'v'}_B$, $\overline{w'\theta'}_B$, and σ_B to be due to sampling of a stationary process. Following Lumley and Panofsky (1964) the variability of a Gaussian quantity X is expected to scale as

TABLE III

Dimensionless coefficients α_X from $\sigma_X/\overline{X} = \alpha_X(z/U\Upsilon)^{1/2}$ where X is the quantity in the first column, z is the measurement height, U is the mean wind speed and Υ is the measurement duration. The values α_S are from Sreenivasan et al. (1978). α_{MIUU}, α_{R2} and α_{R3} are calculated from the data of Högström and Smedman (2004) for MIUU, Gill R2 and Gill R3 anemometers. Subscript C refers to the mean values from the R2/R3 comparison.

X	α	α_S	α_{MIUU}	α_{R3}	α_{R2}	α_{RC}
σ_u	4.70	1.73	1.60	3.76	2.21	2.67
σ_v	8.45	–	1.45	4.01	2.92	3.55
σ_w	1.95	0.87	1.84	2.45	1.47	2.19
$\sigma_{\theta s}$	3.12	2.12	3.44	4.29	3.64	8.30
$-\overline{w'u'}$	7.38	5.5	6.11	9.41	8.32	7.70
u_*^2	7.22	–	6.27	9.57	8.08	7.11
$-\overline{w'v'}$	10.23	–	–	–	–	–
$\overline{w'\theta'}$	8.85	8.0	5.12	11.45	5.94	14.80

$$\sigma_X/\overline{X} = \alpha_X(z/U\Upsilon)^{1/2}, \tag{9}$$

where α_X is a constant, and $\Upsilon = 1800\,\mathrm{s}$ is the duration of measurements. The α coefficients are given in Table III. Using the average 6.5-m wind speed for the stationary period, we find $\alpha_{-\overline{w'u'}} = 7.38$. This is 34% higher than the value reported by SCA78, and 13% above that of Donelan (1990) based on 7 hours of data from a bivane anemometer. The variability of the cross-wind stress (normalised by $-\overline{w'u'}$, since the mean of $-\overline{w'v'}$ is near zero) is 50% higher, with $\alpha_{-\overline{w'v'}} = 10.23$. For the stress magnitude, u_*^2, we find $\alpha_{u_*^2} = 7.22$. Finally, $\alpha_{\overline{w'\theta'}} = 8.85$, 10% higher than the value reported by SCA78. The coefficients for the velocity moments are roughly double those of SCA78.

5. Discussion and Conclusions

The studies of SCA78, Donelan (1990), and the present work take the approach of looking at the variability of various turbulent quantities within a single long stationary record. They assumed the measured variability to be associated with sampling variability alone.

Högström and Smedman (2004) took a different approach. They carried out a series of four experiments, in each of which two or more anemometers were deployed close together. They then looked at the variability of the difference between the measured quantities, which they took to be representative of the instrument error. In the first test carried out at 1.56-m height over land (heath), three MIUU hot film turbulence sensors were deployed, spaced about 3 m apart. By assuming *rms* differences between pairs of sensors to be divided equally, estimates of the MIUU sensor error were found for various fluxes and moments. For instance, the error $\sigma_X/\overline{X}$ for $X=-\overline{w'u'}$ was found to be 8%. Subsequent tests were then carried out between a MIUU sensor and a Gill 1012R2, a MIUU sensor and a Gill 1012R3, and the R2 and R3. Each of these tests were carried out at 10-m elevation either over water or farmland, with the sensors separated by 1.35 m (Högström, 2005, personal communication). In analysing the MIUU/Gill comparisons, the MIUU error found from the first tests was removed from the total error to arrive at the R2 or R3 error. The resulting R2 and R3 errors were found to be roughly three times higher those that of the MIUU hot film sensor.

Furthermore, these values are significantly larger than the variability in $-\overline{w'u'}_B$ estimated during AWE with a R2A anemometer, even after accounting for the differences in sensor height and wind speed. Given that a side-by-side comparison of sensors will filter out the effects of natural variability on scales much larger than the separation distance, the opposite would have been expected. Clearly the estimates in the errors in the R2/R3 intercomparison should be consistent with the errors from the R2 and R3 when compared with the MIUU. However, this is not the case. For instance the R2 and R3 errors for $-\overline{w'u'}$ were estimated to be 35% and 23% respectively when compared against the MIUU. However, the direct comparison of the R2 and R3 yielded a total error in the two $-\overline{w'u'}$ values of 26%. Similar conclusions follow for the other fluxes and moments.

This inconsistency could arise from the assumption that the *rms* difference between two sensors arises entirely from instrument error. Indeed even at O(1 m) separation, some of the measured differences will be associated with sampling variability (Dyer et al., 1982). Since sampling variability scales with $(z/U\Upsilon)^{1/2}$ (from Equation (9)) the MIUU intercomparison at 1.56-m elevation would exhibit $(10/1.56)^{1/2}\approx 2.5$ times less sampling variability than the other comparisons carried out at 10 m. If this correction, plus a factor accounting for the mean wind speed differences, are made to the MIUU sensor error (i.e. assuming all the error to be sampling variability), the estimated R3 errors are reduced by about 10%, and the R2 errors by 25%. Alternatively, if we assume the errors in the R2 and R3 (sensors with similar head designs) to be roughly the same, we can use the R2/R3 intercomparison to constrain the error estimates for the R2 and R3. This typically results in a reduction in the R3 errors by 20%.

In Table III, we give estimates of the α coefficients calculated from the Högström and Smedman (2004) data. Although this assumes (incorrectly) that all the difference between sensors arises from sampling variability, it allows for a comparison with the estimates found in the AWE study. The final column in Table III gives the value from the R2/R3 intercomparison α_{RC}, assuming equal errors in the two. We consider the minimum of α_{R3} (or α_{R2}) and α_{RC} to be the best estimate for the R3 (or R2) error. For σ_w, σ_θ, u_*, $-\overline{w'u'}$, and $-\overline{w'\theta'}$ these latter values are close to those found in the AWE study. For the horizontal velocity moments, σ_u and σ_v, the variability in AWE is roughly double that observed by any of the MIUU/R2/R3 sensors. This is consistent with the horizontal velocity spectra being dominated by larger spatial scales – variability missed in the intercomparison.

We have analysed the sampling variability of the turbulent momentum and heat fluxes, along with second-order moments, during a week-long stationary period. The dimensionless variability $\sigma_X/\overline{X}$ in $-\overline{w'u'}$, u_*^2, $-\overline{w'\theta'}$, σ_w and σ_θ is found to agree with the constrained estimates of Högström and Smedman (2004), but are significantly larger those of SCA78 (except for $-\overline{w'\theta'}$, which agrees with SCA78).

Following Krogstad et al. (1999), the estimated sampling variability can be used to define confidence regions in a scatter plot. For instance, Figure 8d shows a scatter plot of predicted bulk versus measured heat flux. The dashed lines shown on the plot indicate the 90% confidence region using Equation (9) with $\alpha_{w\theta} = 8.85$ and the mean speed for the experiment. This assumes equal variability on both axes. Considering the full unstable dataset, 75% of the data fall within the 90% confidence limits; if only nighttime data are included, the figure rises to 85%. However, for the stable data only 52% of the data fall in the expected range. From this we conclude that while the bulk formula does not adequately model the stable data, the scatter among the unstable data is consistent with sampling variability. For the daytime unstable data, the increased variability is likely attributable to errors in water temperature. A similar analysis of bulk, wave-age and wave-steepness models on the momentum flux for AWE and other experiments is given in Drennan et al. (2005).

Finally, our analysis has revealed the first *in situ* evidence for the steering of wind stress by surface currents. Although it is usually assumed that surface currents are weak and can be ignored relative to U_{10N}, it was shown that even a weak surface current perpendicular to the wind can modify the stress direction. This might explain some of the scatter present in other studies where the stress direction has been related to the swell direction or stability.

Acknowledgements

Support from ONR (N00014-00-1-0594 to WMD and N00014-98-1-0818 and N00014-02-1-0972 to LKS) is gratefully acknowledged. We thank the following for their support with various aspects of this work: Tom Cook, Manhar Dhanak, Joe Gabriele, Brian Haus, Delphine Icard, Jorge Martinez, Mike Rebozo, and the captain and crew of the R/V Walton Smith. We also thank Professor Ulf Högström and two reviewers for their comments on the manuscript. Jose Vasquez of the City of Hollywood Beach and Jim Davis of Broward County Parks and Recreation kindly allowed access to the property on the beach in Hollywood. Lou Fisher and Mark Taynton of the Florida Department of Environmental Protection, and Karen Moody of the Department of Florida Fish and Wildlife Commission provided valuable assistance to the project. June Carpenter allowed us access to her beach house for OSCR operations. Renate Skinner and Sid Leve permitted us to use the beach at the John U. Lloyd State Park. Bill Venezia at the US Navy South Florida Testing Facility provided logistical support for our operations at the park. ADCP data are courtesy of Bob Weisberg (USF) and Alex Soloviev (Nova).

References

Anctil, F., Donelan, M. A., Drennan, W. M., and Graber, H. C.: 1994, 'Eddy Correlation Measurements of Air–Sea Fluxes from a Discus Buoy', *J. Atmos. Ocean. Technol.* **11**, 1144–1150.

Capon, J.: 1969, 'High-resolution Frequency-Wavenumber Spectrum Analysis', *Proc. IEEE* **57**, 1408–1418.

Cornillon, P. and Park, K.-A.: 2001, 'Warm Core Ring Velocities Inferred from NSCAT', *Geophys. Res. Lett.* **28**, 575–578.

DeCosmo, J., Katsaros, K. B., Smith, S. D., Anderson, R. J., Oost, W. A., Bumke, K., and Chadwick, H.: 1996, 'Air–Sea Exchange of Water Vapor and Sensible Heat: The Humidity Exchange Over the Sea (HEXOS) results', *J. Geophys. Res.* **101**, 12001–12016.

Dhanak, M. R., An, P. E., and Holappa, K.: 2001, 'An AUV Survey in the Littoral Zone: Small-scale Subsurface Variability Accompanying Synoptic Observations of Surface Currents', *IEEE J. Oceanic Eng.* **24**, 752–768.

Donelan, M. A.: 1990, 'Air–Sea Interaction', in B. LeMéhauté and D. Hanes (eds.), *The Sea: Ocean Engineering Science,* Vol. 9, John Wiley and Sons, Inc., New York, pp. 239–292.

Donelan, M. A., Hamilton, J., and Hui, W. H.: 1985, 'Directional Spectra of Wind Generated Waves', *Phil. Trans. R. Soc. London* **A315**, 509–562.

Drennan, W. M., Donelan, M. A., Madsen, N., Katsaros, K. B., Terray, E. A., and Flagg, C. N.: 1994, 'Directional Wave Spectra from a Swath Ship at Sea', *J. Atmos. Ocean. Technol.* **11**, 1109–1116.

Drennan, W. M., Graber, H. C., Hauser, D., and Quentin, C.: 2003, 'On the Wave Age Dependence of Wind Stress over Pure Wind Seas', *J. Geophys. Res.* **108**(C3), 8062, doi:10.1029/2000JC000715.

Drennan, W. M., Taylor, P. K., and Yelland, M. J.: 2005, 'Parameterizing the Sea Surface Roughness', *J. Phys. Oceanogr.* **35**, 835–848.

Dupuis, H., Guérin, C., Hauser, D., Weill, A., Nacass, P., Drennan, W. M., Cloché, S., and Graber, H. C.: 2003, 'Impact of Flow Distortion Corrections on Turbulent Fluxes Estimated by the Inertial Dissipation Method during the FETCH Experiment on R/V L'Atalante', *J. Geophys. Res.* **108** (C3), 8064, doi:10.1029/2001JC001075.

Dupuis, H., Taylor, P. K., Weill, A., and Katsaros, K.: 1997, 'Inertial Dissipation Method Applied to Derive Turbulent Fluxes over the Ocean During the Surface of the Ocean, Fluxes and Interactions with the Atmosphere/Atlantic Stratocumulus Transition Experiment (SOFIA/ASTEX) and Structure des Echanges Mer-Atmosphere, Proprietes des Hétérogeneites Océaniques: Recherche Experimentale (SEMAPHORE) Experiments with Low to Moderate Wind Speeds', *J. Geophys. Res.* **102**, 21115–21129.

Dyer, A. J., Garratt, J. R., Francey, R. J., McIlroy, I. C., Bacon, N. E., Hyson, P., Bradley, E. F., Denmead, O. T., Tsvang, L. R., Volkov, Y. A., Koprov, B. M., Elagina, L. G., Sasashi, K., Monji, N., Hanafusa, T., Tsukamoto, O., Frenzen, P., Hicks, B. B., Wesely, M., Miyake, M., and Shaw, W.: 1982, 'An International Turbulence Comparison Experiment (ITCE 1976)', *Boundary-Layer Meteorol.* **24**, 181–209.

Geernaert, G. L., Davidson, K. L., Larsen, S. E., and Mikkelson, T.: 1988, 'Wind Stress Measurements During the Tower Ocean Wave and Radar Dependence Experiment', *J. Geophys. Res.* **93**, 13913–13923.

Geernaert, G. L., Hansen, F., Courtney, M., and Herbers, T.: 1993, 'Directional Attributes of the Ocean Surface Wind Stress Vector', *J. Geophys. Res.* **98**, 16571–16582.

Gerling, T. W.: 1992, 'Partitioning Sequences and Arrays of Directional Ocean Wave Spectra into Component Wave Systems', *J. Atmos. Ocean. Technol.* **9**, 444–458.

Graber, H. C., Terray, E. A., Donelan, M. A., Drennan, W. M., Van Leer, J. C., and Peters, D. B.: 2000, 'ASIS – A New Air–Sea Interaction Spar Buoy: Design and Performance at sea', *J. Atmos. Ocean. Technol.* **17**, 708–720.

Grachev, A. A., Fairall, C. W., Hare, J. E., Edson, J. B., and Miller, S. D.: 2003, 'Wind Stress Vector over Ocean Waves', *J. Phys. Oceanogr.* **33**, 2408–2429.

Halpern, D.: 1988, 'Moored Surface Wind Observations at Four Sites along the Pacific Equator between 140° and 95°W', *J. Climate* **1**, 1251–1260.

Högström, U. and Smedman, A. S.: 2004, 'Accuracy of Sonic Anemometers: Laminar Wind-tunnel Calibrations Compared to Atmospheric *In Situ* Calibrations Against A Reference Instrument', *Boundary-Layer Meteorol.* **111**, 33–54.

Kaimal, J. C. and Gaynor, J. E.: 1991, 'Another Look at Sonic Anemometry', *Boundary-Layer Meteorol.* **56**, 401–410.

Katsaros, K. B.: 1980, 'The Aqueous Thermal Boundary Layer', *Boundary-Layer Meteorol.* **18**, 107–127.

Katsaros, K. B., Donelan, M. A., and Drennan, W. M.: 1993, 'Flux Measurements from a Swath Ship in SWADE', *J. Mar. Sys.* **4**, 117–132.

Kitaigorodskii, S. A. and Volkov, Y. A.: 1965, 'On the Roughness Parameter of the Sea Surface and the Calculation of Momentum Flux in the Near-Water Layer of the Atmosphere', *Izv., Atmos. and Oceanic Phys.* **1**, 973–988.

Krogstad, H. E., Wolf, J., Thompson, S. P., and Wyatt, L. R.: 1999, 'Methods for Intercomparison of Wave Measurements', *Coastal Eng.* **37**, 235–257.

Large, W. G. and Pond, S.: 1982, 'Sensible and Latent Heat Flux Measurements over the Ocean', *J. Phys. Oceanogr.* **12**, 464–482.

Larsén, X. G., Smedman, A. S., and Högström, U.: 2004, 'Air–Sea Exchange of Sensible Heat Over the Baltic Sea', *Quart. J. Roy. Meteorol. Soc. B* **130**, 519–539.

Lumley, J. L. and Panofsky, H. A.: 1964, *The Structure of Atmospheric Turbulence*, Interscience, New York, 239 pp.

Martinez-Pedraja, J., Shay, L. K., Cook, T. M., and Haus, B. K.: 2004, 'Very High Frequency Surface Current Measurement along the Inshore Boundary of the Florida Current during NRL 2001', *RSMAS Technical Report 2004–03*, Rosenstiel School of Marine and Atmosphere Science, University of Miami, Miami, FL 33149, 30 pp.

Pedreros, R., Dardier, G., Dupuis, H., Graber, H. C., Drennan, W. M., Weill, A., Guérin, C., and Nacass, P.: 2003, 'Momentum and Heat Fluxes via the Eddy Correlation Method on the R/V L'Atalante and an ASIS buoy', *J. Geophys. Res.* **108**(C11), 3339, doi:10.1029/2002JC001449.

Peters, H., Shay, L. K., Mariano, A. J., and Cook, T. M.: 2002, 'Current Variability on a Narrow Shelf with Large Ambient Vorticity', *J. Geophys. Res.* **107**(C8), doi:10.1029/2001JC000813.

Pettersson, H., Graber, H. C., Hauser, D., Quentin, C., Kahma, K. K., Drennan, W. M., and Donelan, M. A.: 2003, 'Directional Wave Measurements from Three Wave Sensors during the FETCH Experiment', *J. Geophys. Res.* **108**(C3), 8061, doi:10.1029/2001JC001164.

Rieder, K. F., Smith, J. A., and Weller, R. A.: 1994, 'Observed Directional Characteristics of the Wind, Wind Stress and Surface Waves on the Open Ocean', *J. Geophys. Res.* **99**, 22589–22596.

Schotanus, P., Nieuwstadt, F. T. M., and DeBruin, H. A. R.: 1983, 'Temperature Measurement with a Sonic Anemometer and its Application to Heat and Moisture Fluctuations', *Boundary-Layer Meteorol.* **26**, 81–93.

Shay, L. K., Cook, T. M., Peters, H., Mariano, A. J., Weisberg, R., An, P. E., Soloviev, A., and Luther, M.: 2002, 'Very High Frequency Radar Mapping of Surface Currents', *IEEE J. Oceanic Eng.* **27**, 155–169.

Shay, L. K., Cook, T. M., and An, P. E.: 2003, 'Submesoscale Coastal Ocean Flows Detected by VHF Radar and Autonomous Underwater Vehicles', *J. Atmos. Oceanic Technol.* **20**, 1583–1599.

Smith, S. D.: 1980, 'Wind Stress and Heat Flux over the Ocean in Gale Force Winds', *J. Phys. Oceanogr.* **10**, 709–726.

Smith, S. D.: 1989, 'Water Vapor Flux at the Sea Surface', *Boundary-Layer Meteorol.* **47**, 277–293.

Soloviev, A. V., Walker, R. J., Weisberg, R. W., and Luther, M. E.: 2003, 'Coastal Observatory Investigates Energetic Current Oscillations on Southeast Florida Shelf', *EOS, Trans. Amer. Geophys. Union* **84**, 441–450.

Sreenivasan, K. R., Chambers A. J., and Antonia, R. A.: 1978, 'Accuracy of Moments of Velocity and Scalar Fluctuations in the Atmospheric Surface Layer', *Boundary-Layer Meteorol.* **14**, 341–359.

Stewart, R. H. and Joy, J. W.: 1974, 'HF Radio Measurements of Surface Currents', *Deep Sea Res.* **21**, 1039–1049.

Stull, R. B.: 1988, *An Introduction to Boundary Layer Meteorology*, Kluwer Academic Publishers, Dordrecht, 666 pp.

Venezia, W. et al.: 2003, 'SFOMC: A successful Navy and Academic Partnership Providing Sustained Ocean Observation Capabilities in Florida Straits', *Marine Tech. Soc.* **37**, 81–91.

Wyngaard, J. C.: 1973, 'On Surface Layer Turbulence', in D. A. Haugen (ed.), *Workshop on Micrometeorology*, Amer. Meteorol. Soc., Boston, pp. 101–149.

Zemba, J. and Friehe, C. A.: 1987, 'The Marine Atmospheric Boundary Layer Jet in the Coastal Ocean Dynamics Experiment', *J. Geophys. Res.* **92**, 1489–1496.